Photochemical Reaction Mechanism of UV-B-Induced Monomerization of UVR8 Dimers as the First Signaling Event in UV-B-Regulated Gene Expression in Plants
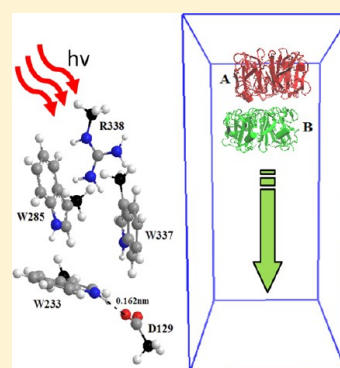
Min Wu,[†] Åke Strid,[‡] and Leif A. Eriksson*,[†]

[†]Department of Chemistry and Molecular Biology, University of Gothenburg, SE-412 96 Göteborg, Sweden
[‡]School of Science and Technology, Örebro University, SE-70182 Örebro, Sweden

S *Supporting Information*

ABSTRACT: The *Arabidopsis thaliana* UV RESISTANCE LOCUS8 (UVR8) protein has been identified to specifically mediate photomorphogenic UV-B responses by acting as a UV-B photoreceptor. The dimeric structure of the UVR8 protein dissociates into signaling-active monomers upon UV-B exposure, and the monomers rapidly interact with downstream signaling components to regulate gene expression. UVR8 monomers revert to dimers in the absence of UV-B radiation, thereby reversing transcription activation. UVR8 amino acid residues W233 and W285 have been identified to play critical roles in the UVR8 dimer for the response to UV-B irradiation. In the present work, the photoreaction mechanism for UVR8 monomerization is explored with quantum chemical cluster calculations and evaluated by molecular dynamics simulations using the wild-type UVR8 dimer and novel force field parameters developed for intermediate radicals formed in the photochemical process. Three different models are investigated, which show that the preferred mechanism for UVR8 monomerization involves electron transfer from residue W233 to W285 and onward to R338 initiated by UV-B irradiation, coupled to simultaneous proton transfer from W233 to D129 leading to the formation of protonated D129, a deprotonated W233 radical, and a neutral R338 radical. Due to the formation of the neutral R338 radical, salt bridges involving this residue are disrupted together with the concomitant interruption of several other key salt bridges R286-D96, R286-D107, R338-D44, R354-E43, and R354-E53. The resulting large decrease in protein–protein interaction energy arising from this sequence of events leads to the monomerization of the UVR8 dimer. The mechanism presented is in accord with all experimental data available to date.

1. INTRODUCTION

UV-B radiation (UV-B; 280−315 nm) is part of the solar radiation reaching the surface of the earth and inducing diverse morphological and deleterious effects on biological molecules and therefore also on cells and living organisms, including plants.[1,2] Plant responses include molecular and cellular changes such photolysis of pyridoxine (vitamin B6),[3] accumulation of flavonoid-derived pigments,[4] induction of UV-B responsive genes,[5] and alteration of plant morphology resulting in decreased leaf size, increased leaf thickness, increased branching, and deposition of wax on the upper cuticle of leaves.[6]

The *Arabidopsis thaliana* UV RESISTANCE LOCUS8 (UVR8) protein has been identified to specifically mediate photomorphogenic UV-B responses by acting as a UV-B photoreceptor.[7−11] UVR8 is involved in orchestrating the expression of more than 100 genes[7,10,12,13] and has been suggested to have appeared early in the evolution of plants, for them to survive exposure to the UV-B fraction of the sunlight before the formation of the dioxygen rich atmosphere and the ozone-containing stratosphere.[14,15] An action spectrum for UVR8 function indicates that the major UV absorption of the UVR8 protein is around 280 nm, but the most physiologically

relevant responses are induced by absorption occurring with a minor absorption peak at ∼300 nm. Upon absorption of UV-B by UVR8, substantial mRNA transcript accumulation occurs for a number of genes, e.g., the photomorphogenically important transcription factor HY5.[16]

The UVR8 protein is a dimer located in the cytosol and dissociates into a signaling-active monomer upon UV-B exposure.[15] The UVB-induced UVR8 monomers rapidly reverse to dimers in vivo upon cessation of UV-B exposure, indicating a reversible process.[17] The explicit reaction mechanism of the UV-B-induced reaction is as yet unclear. Residues W285 and W233 have been identified to be critical in inducing the monomerization reaction in response to UV-B irradiation.[8,11,18] Tryptophan is an amino acid that is frequently involved in proton-coupled electron transfer under physiological conditions.[19,20] Electron transfer is central to a vast array of biological processes and often involves the formation of amino acid radical intermediates. It has been proposed that

biological electron transfer can occur over distances as long as 14 Å in the presence of the radical intermediates.[21]

The 3D structures of the core domain of the *A. thaliana* wild-type UVR8 and its W285F and W285A single mutants have recently been published.[8,11] The 11 most N-terminal amino acids and the 55 C-terminal amino acids are missing from the crystal structures. However, the N-terminal 23 amino acids have in another study been identified to play a key role in the UVR8 nuclear import mechanism.[22] The C-terminal 27 amino acid sequence 397−423 of UVR8 has in turn been identified to be necessary and sufficient for UVR8 interaction with the seven-bladed WD propeller domain of the E3 ubiquitin ligase CONSTITUTIVELY PHOTOMORPHOGENIC 1 (COP1),[23] which is known not only as a repressor of photomorphogenesis in darkness but also as a positive regulator of UV-B specific responses.[24,25] The UVR8/COP1 interaction is crucial for the activation of the UV-B photomorphogenic pathway and UV-B-dependent gene expression.[10,13,25] In a previous study of ours, the de novo folds of the UVR8[397−423] peptide were predicted using computational modeling. An α-helix structure was found to be the preferred fold in the UVR8 sequence 404−409, and residues V410 and P411 were, using a computational docking approach, predicted to interact with COP1 by hydrophobic interactions.[26]

Thirteen tryptophan residues are included in the crystal structure of UVR8, and are highly conserved among plant species.[8,11,15,18] Residues W39, W92, W144, W196, W300, and W352 were identified to take part in the maintenance of the WD40 structure by hydrogen bonds and hydrophobic interactions,[27] and residues W94, W198, W233, W250, W285, W302, and W337 are positionally located at the dimeric interface. W285A and W39A mutants were constitutive monomers whereas W233F and W285F mutants were constitutive dimers, both in the absence and in the presence of UV-B.[11,15,27] For the W233A and W337A mutants, both dimeric and monomeric structures were observed in the absence of UV-B.[27] The dominating quaternary structures of all these UVR8 mutants were determined using gel filtration. Strong hydrogen bonding interaction was seen between residue W233 and D129 in the wild-type crystal structure, which indicates that residue D129 may serve as an acceptor of a proton from W233.[11]

Several salt bridges involving arginines R146, R200, R286, R338, and R354, aspartic acids D107 and D96, and glutamic acids E53, E43, E158, and E182 were found in the dimer crystal structure.[8,11] Single mutants R286A and R338A were constitutive monomers in the absence of UV-B[11] as were the double mutants D96N/D107N, R146A/R286A, and R286A/R338A,[8] whereas single mutants R146A, R200A, and R354A were dimers in the absence of UV-B and underwent UV-B-induced monomerization.[11]

In our previous papers, quantum chemical calculations of absorption spectra of a large model cluster involving twelve residues, as well as several smaller amino acid cluster fragments, reveal that W233 and W285 (in the presence of R234, R286, and R338) are essential for the absorption at the wavelengths around 300 nm found in the action spectrum.[18] Normal molecular dynamics (MD) simulations and steered MD (SMD) simulations with umbrella sampling were employed in another of our studies to investigate the influence of single mutations R286A and R338A and the double mutation R286A/R338A on the structure of the UVR8 dimer. The binding energies between the UVR8 monomers were reduced by 40%, 56%, and

65%, respectively, and the center of mass (COM) distances at the energy minima increased by 0.01, 0.11, and 0.18 nm, respectively, relative to the wild-type UVR8 dimer. It was thus concluded that both R286 and R338 are important residues for the stabilization of the dimeric structure of UVR8. Considering that the COM distances between the monomers only increased by 0.01 nm at the energy minimum point for the single mutant R286A compared with the case of the wild-type, we furthermore concluded that both the monomeric and the dimeric UVR8 structures may exist for the R286A single mutant.[28]

In the current work, we explore the underlying molecular mechanism of the UV-B-induced monomerization of the UVR8 dimer. For the quantum calculations we employ a cluster approach based on the UVR8 wild-type and W285F mutant crystal structures in the ground state and first excited triplet state to investigate different mechanistic hypotheses. These are followed by MD and SMD simulations to perform UVR8 dimer stability analyses that provide further insight into what mechanism that is the more probable. The $\Delta\Delta E_{bind}$ cutoff for monomerization of the UVR8 dimer is further determined by using receiver operating characteristic (ROC) curves, based on simulation of seven single and three double UVR8 mutants, to determine which of our suggested mechanisms that upon UV-B absorption will induce complete monomerization of the UVR8 dimer.

2. METHODOLOGY

2.1. Cluster Preparation. Compared to the Cα root-mean-square deviation (Cα-RMSD) of the wild-type crystal structure (PDB code: 4DNW),[11] the Cα-RMSD of the UVR8[W285A] monomer crystal structure (PDB code: 4DNU)[11] is only 0.025 nm and is mainly caused by a movement of the indole ring of residue W337 to occupy the vacated space resulting from the W285A mutation. In addition, the hydrogen bonding interaction between W233 and D129 is interrupted by a rotation of the W233 indole ring.[11] Single mutants R286A and R338A are constitutive monomers, indicating that these two residues are critical in the formation of the UVR8 dimeric structure.[11] In a previous study, we found that longer wavelength absorptions of the critical residues W233 and W285 were obtained in the presence of residues R234, R286, and R338, compared to absorptions for tryptophan in solution or clusters that did not contain the arginines.[18] Hence, it is most likely residues R234, R286, R338, W233, W285, W337, and D129 that are involved in the UV-B-induced monomerization mechanism.

The initial structures used for the quantum chemical cluster calculations were taken from the X-ray structures (PDB entries: 4DNW and 4DNV, resolution 1.77 and 2.00 Å, respectively) obtained for *A. thaliana* UVR8.[11] The protonation states of the titratable residues were determined from their pK_a values as calculated by the Protonate 3D program in the MOE2011 package,[29] and hydrogen atoms missing in the crystal structure were added. To determine the influence by the three arginines, clusters including W233, W285/W285F, W337, and D129 together with one of the different single arginines R234, R286, or R338 were cut out from the protonated wild-type/W285F crystal structures (Scheme 1). The D129 residue was modeled in the ionized form and the arginines were assumed to be protonated. W233 is engaged in a hydrogen bond with residue D129. The total size of the models includes 77 and 73 atoms for the wild-type and W285F clusters, respectively.

Scheme 1. Key Systems Including Residues Trp233, Trp285, Trp337, and Asp129 with the Single Arginines (Arg234 in Red, Arg286 in Green, and Arg338 in Blue)[a]
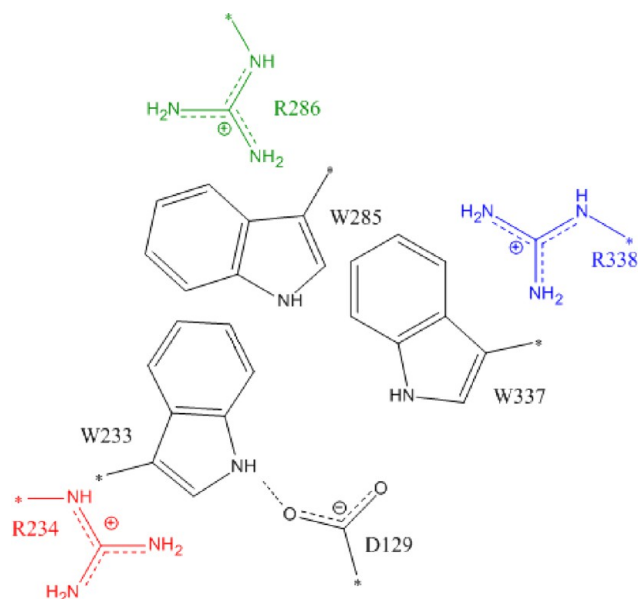
[a]The atoms with asterisks were kept fixed during the structure optimizations.

2.2. Quantum Chemical Calculations. All structures were optimized in the ground state and first excited triplet states at the hybrid B3LYP Hartree-Fork DFT level of theory,[30,31] in conjunction with the 6-31G(d,p) basis set in vacuum. The truncation atoms were kept fixed at their X-ray positions during the geometry optimizations, to keep the optimized structure resembling the experimental one. This is a standard procedure in the cluster approach for modeling enzymes.[32] The frozen atoms are indicated by asterisks in Scheme 1. The accuracy of B3LYP in geometry optimizations of biomolecules is well established and normally provides geometries in very close agreement with experimental data. Harmonic vibrational frequency calculations were performed at the same level on the optimized geometries, to ensure that the systems found were minima on their respective energy surfaces, and to extract zero-point vibrational energies (ZPE) and Gibbs energy contributions at 298 K. To be consistent with our previous study,[18] single-point energy calculations for vertical singlet excitations were calculated at the TD-ωB97xd/6-31G(d,p)[33] level using the TD-DFT approach in vacuum. ωB97xd is an extended version of the long-range corrected ωB97 and ωB97X[34] functionals with an additional empirical dispersion correction and has been shown in general to perform very well in excited state calculations, including long-range charge transfer excitations.[35] All quantum chemical calculations were performed using the Gaussian09 program.[36] Natural bond orbital (NBO) analyses were also performed.[37]

2.3. Molecular Dynamics Simulations. In all the initial structures, the titratable amino acids were assigned their canonical protonation states at pH = 7 by the 3Dprotonate-algorithm in MOE2011.[29] The molecular simulations were carried out using the Gromacs 4.5.5 package.[38,39] The Amber03 force field[40] was employed for all MD simulations and energy minimizations in this work. The force field parameters of the deprotonated tryptophan radical were established by Ante-chamber in the Amber10 package,[41] whereas the force field parameters for the arginine radicals were built at the ab initio HF/6-31G* level with restrained electrostatic potential (RESP) charges.[41,42] For short-range nonbonded interactions, a cutoff of 1.4 nm was used, and long-range electrostatic interactions were calculated using the particle mesh Ewald (PME) algorithm.[43,44] Dispersion corrections were applied to the energy and pressure terms to account for the truncation of the van der Waals terms, and periodic boundary conditions were applied in all directions.

To generate equilibrated starting structures for the SMD pulling simulations, photoreacted structures were generated using the crystal structure of the wild-type UVR8 dimer, solvated by TIP3P water molecules, and with Na$^+$ counterions added as required to neutralize the total charge of the systems.
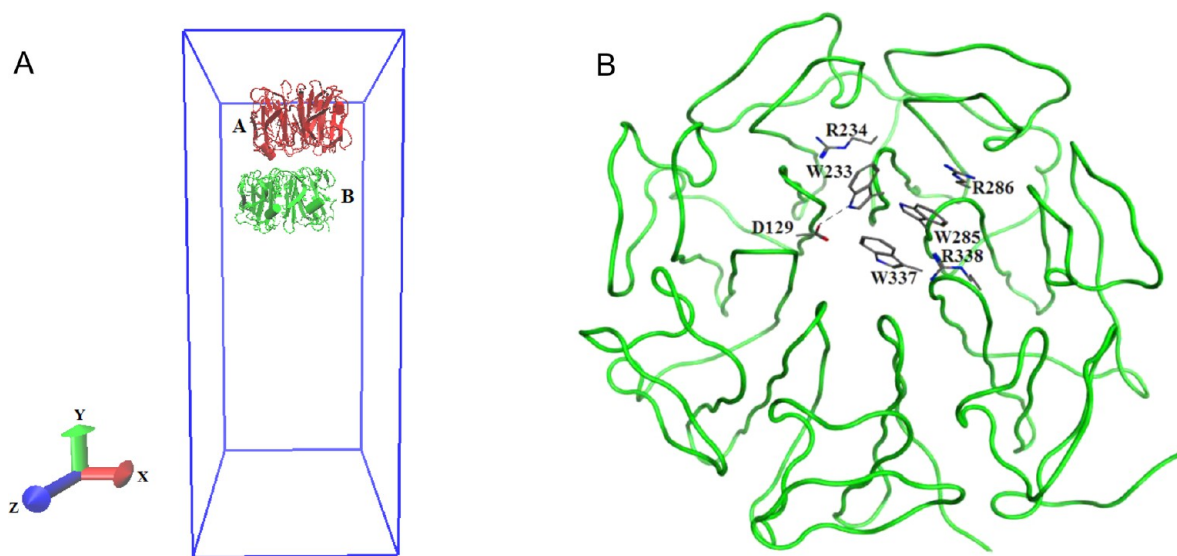

Figure 1. (A) Side view of the wild-type UVR8 dimer in a 8 × 20 × 8 nm box with each monomer labeled according to the nomenclature used in the paper. Pulling is done in the negative direction along the y-axis. Water molecules and counterions are not displayed for clarity. (B) Top view of monomer B showing the key interfacial residues.

Scheme 2. Three Hypothetical Photoinduced Reaction Mechanism Pathways Triggering UVR8 Dimer Monomerization, Investigated in This Study
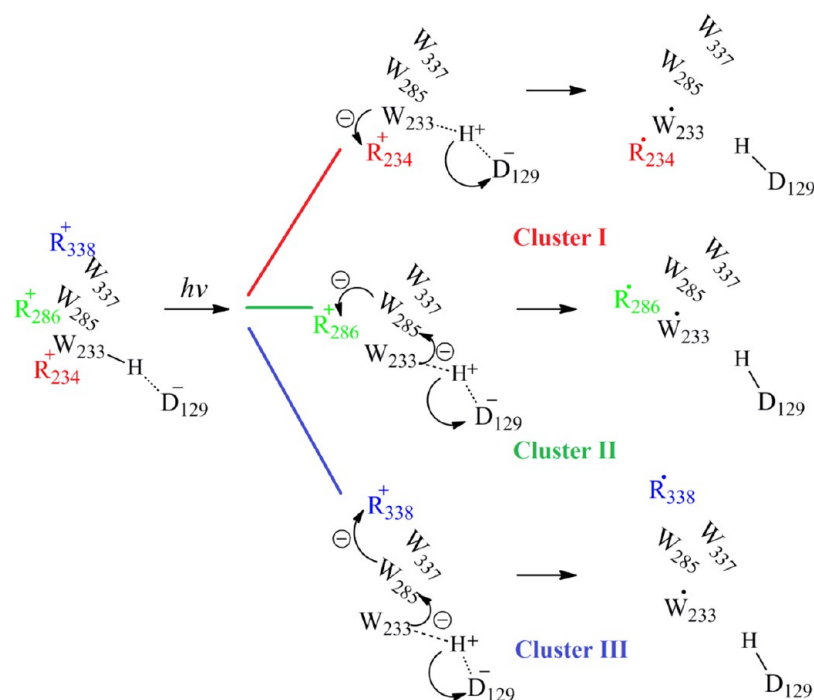
Following steepest descent minimizations, each system was equilibrated with position restraints applied to peptide heavy atoms for 100 ps under a constant volume (NVT) ensemble, with protein and nonprotein atoms coupled to separate constant temperature thermostats (310 K) using the Berendsen weak coupling method.[45] This was followed by 100 ps constant pressure (NPT) equilibration, using a weak coupling to maintain the pressure isotropically at 1.0 bar. The final MD simulations were performed for 100 ns with the NPT ensemble in the absence of any restraints. For this data collection period, the Nosé–Hoover thermostat[46,47] was used to maintain temperature, and the Parrinello–Rahman barostat[48,49] was used to isotropically regulate the pressure.

The structures taken at the end of each trajectory were used as starting points for the pulling simulations. The A monomers were superposed whereafter each system was placed in a rectangular box with dimensions $8 \times 20 \times 8$ nm, sufficient to satisfy the minimum image convention and provide space for pulling simulations to take place in the negative y-direction (Figure 1). As before, the structures were solvated with TIP3P water molecules and Na$^+$ counterions were added as required to neutralize the total charge of the systems. Equilibration was performed for 500 ps in an NPT ensemble, using the same methodology as described before with position restraints applied to the peptide heavy atoms.

Following equilibration, restraints were removed from monomer B (Figure 1), and monomer A was used as an immobile reference for the pulling simulations. For each of the systems, monomer B was pulled away from the core structure in the negative direction along the y-axis for over 5000 ps, using a spring constant of 240 (kcal/mol)/nm^2 and a pull rate of 0.001 nm/ps. The final center of mass (COM) distance between monomers A and B was approximately 5.5 nm. Each system has around 10 000 atoms in the protein molecules, along with approximately 25 000 solvent molecules in the MD simulations and 40 000 solvent molecules in the SMD simulations.

2.4. Receiver Operating Characteristic (ROC) Curve. ROC curves illustrate the performance of binary classifier systems as the discrimination threshold is varied.[50] ROC curves have been used in various research fields including medicine, biometrics and drug discovery, to facilitate accurate decisions by establishing reliable thresholds. Sensitivity (SE), specificity (SP), prediction accuracy (ACC), and the Matthew's correlation coefficient (MCC) are the main characteristic features of such tests. The formalisms as applied in the current context are shown in eqs 1–4. TD, FD, TM, and FM are defined as the numbers of true dimers, false dimers, true monomers and false monomers, respectively. The predictive performance is usually evaluated in terms of the area under the ROC curve (AUC). The closer AUC is to 1, the better is the performance of the classification.

$$SE = \frac{TM}{TM + FD} \tag{1}$$

$$SP = \frac{TD}{TD + FM} \tag{2}$$

$$ACC = \frac{TD + TM}{TD + FD + TM + FM} \tag{3}$$

$$MCC = \frac{TD \times TM - FD \times FM}{\sqrt{(TD + FD)(TD + FM)(TM + FD)(TM + FM)}} \tag{4}$$

3. RESULTS AND DISCUSSIONS

3.1. Reaction Mechanism Hypothesis As Derived from Quantum Chemical Calculations. Three clusters were

Table 1. Longest Absorption Wavelengths (>245.5 nm) and Their Oscillator Strengths (f), Computed for the Wild-Type UVR8 Cluster Models

systems[a]	S1/nm (f)	orbital	S2/nm (f)	orbital	S3/nm (f)	orbital	S4/nm (f)	orbital
cluster I	274.4 (0.048)	139 → 142	249.3 (0.053)	141 → 144				
cluster II	280.6 (0.070)	140 → 145	247.7 (0.067)	138 → 146				
cluster III	276.5 (0.033)	140 → 143	274.4 (0.036)	135 → 143	267.0 (0.038)	140 → 147	263.5 (0.075)	136→144
free tryptophan	245.5 (0.061)		240.3 (0.063)		191.9 (0.616)			

[a]Cluster I includes residues W233, W285, W337, D129, and R234. Cluster II includes residues W233, W285, W337, D129, and R286. Cluster III includes residues W233, W285, W337, D129, and R337. These cluster labels (Scheme 2) are used throughout the paper.
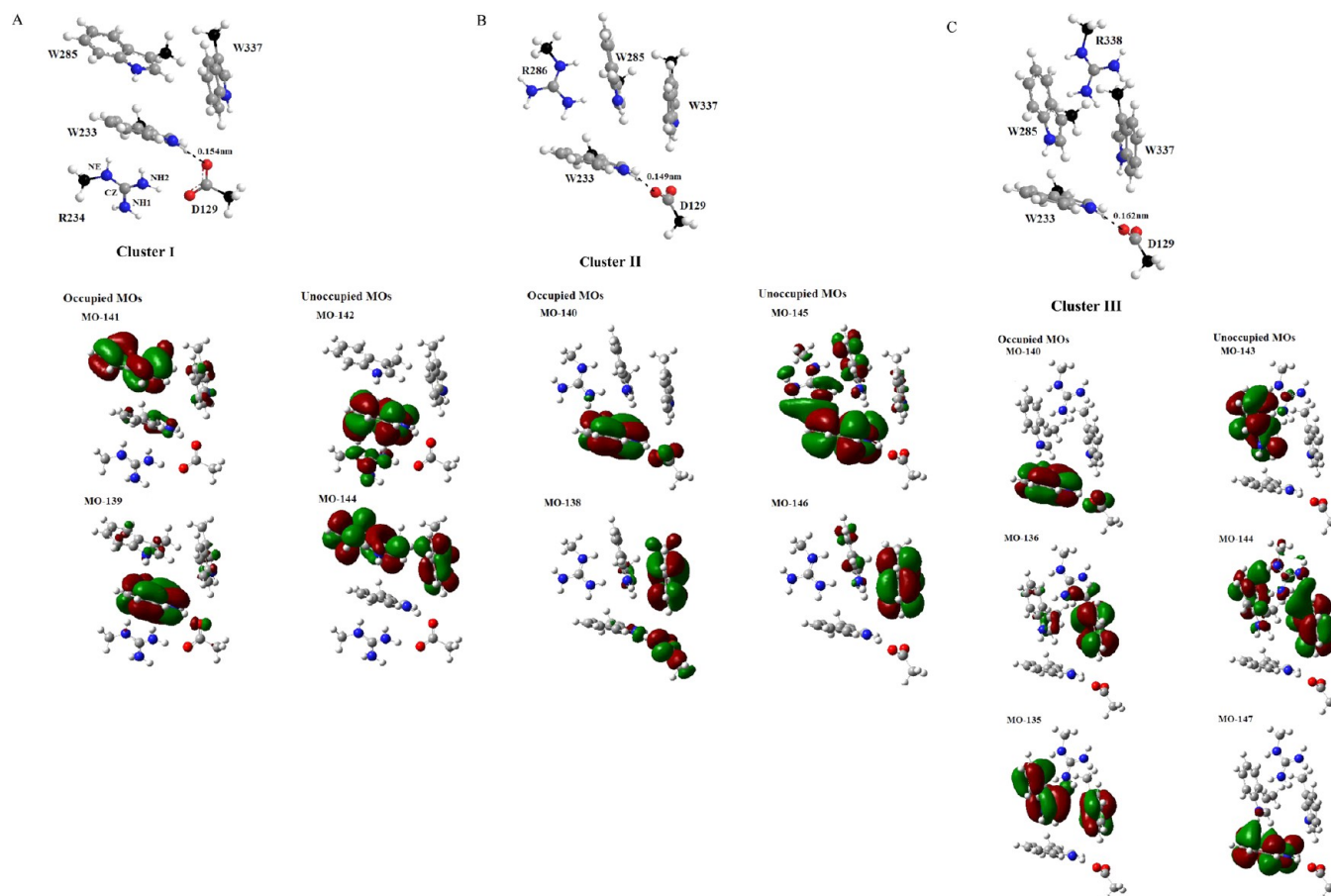
Figure 2. Optimized S_0 structures and the key orbitals involved in absorptions >245.5 nm in (A) cluster I, (B) cluster II, and (C) cluster III of the wild-type UVR8. The images of the optimized structures were produced using ChemDraw12.0, and the molecular orbitals were obtained using Gaussview 5.0 with the isovalue = 0.02.

investigated to explore the molecular mechanism of how the UVR8 dimer can be monomerized by UV-B irradiation. The results concerning the probable reaction mechanism are described as follows and are shown in Scheme 2. In the clusters containing either residue R286 or R338 (clusters II and III), the reaction starts with a UV-B-induced electron transfer from residue W233 via W285, to the arginine residue, with a simultaneous proton transfer from W233 to D129. In the cluster containing R234 (cluster I), the electron is transferred directly from W233 to R234 concomitant with proton transfer from W233 to D129. The protonated D129, the deprotonated W233 tryptophyl radical, and the neutral arginyl radical (at R234, R286, or R338), are finally produced in each cluster. These arginines are involved in salt bridges at the UVR8 dimer interface and can thus be disrupted through charge neutralization.

TD-DFT calculations of vertical singlet excited states based on the optimized structures were performed at the B3LYP/6-31G(d,p)//TD-ωB97xd/6-31G(d,p) level. The key absorption wavelengths and their oscillator strengths are listed in Table 1. The optimized S_0 structures and the key orbitals involved in the electronic excitations are shown in Figure 2. In the clusters, hydrogen bonds are formed between residues W233 and D129 and the distances between the partaking H and O atoms are included in Figure 2. NBO analyses reveal that as expected conjugated bonds are formed between the NH1/NH2/NE-CZ atoms in the guanidinium groups of the arginines with an average of 1.99 electrons, with 60% N character in $sp^{1.7}$ and 40% C character in $sp^{2.0}$ for each C−N bond, and the indol groups of the tryptophans. The atom types NH1, NH2, NE, and CZ represent the N and C atoms in the guanidinium groups of the arginines throughout the paper, as labeled in Figure 2A. The first absorption wavelength for free tryptophan
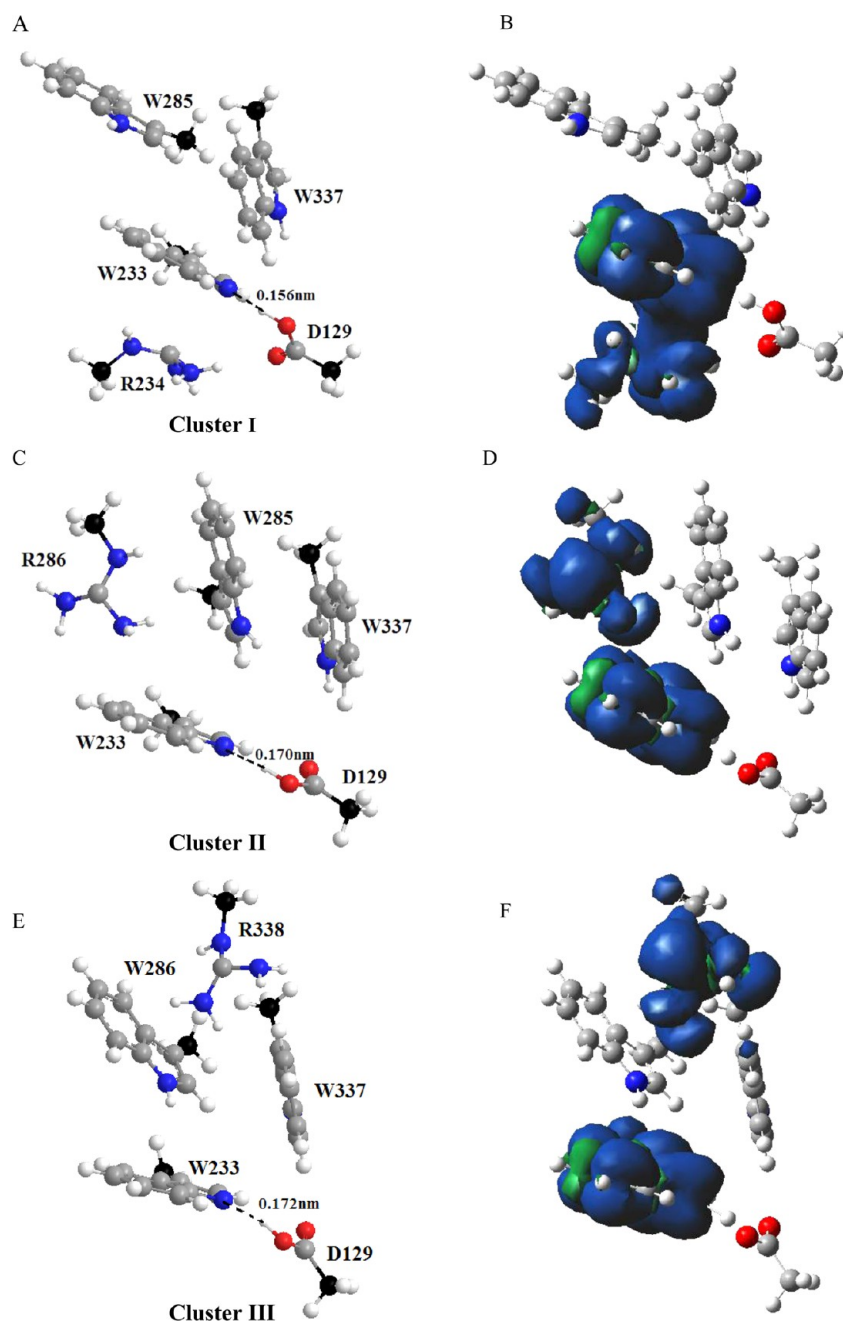
955

dx.doi.org/10.1021/jp4104118 | J. Phys. Chem. B 2014, 118, 951−965

Figure 3. Optimized T_1 structures and spin density distributions of cluster I (A and B), cluster II (C and D), and cluster III (E and F). The images of the optimized structures were produced using ChemDraw12.0, and the spin density distributions (B, D, F) were obtained using Gaussview 5.0 with the isovalue = 0.0004.

is at 245.5 nm at the B3LYP/6-31G//TD-ωB97xd/6-31G(d,p) level. Experimentally, the first absorption wavelength for tryptophan is at 280 nm.[51] At these wavelengths, a 30−35 nm blue shift relative to the experimental results has been found in our previous theoretical studies.[18] An action spectrum of the signaling function of UVR8 indicates that although UVR8 absorption as such is most effective at 280 nm as a result of the high content of tryptophans, the absorption is most physiologically relevant at wavelengths ∼300 nm as contributed by certain tryptophans influenced by the surrounding environment.[16] Hence, only computed absorptions at wavelengths >245.5 nm (corresponding to λ_{exp} > 280 nm), and with oscillator strengths larger than 0.03, are included in Table 1, because this would imply an effect of the surrounding

environment in addition to the chromophore itself. In clusters I and II, the computed absorptions at longest wavelengths occur at approximately 274.4 and 249.3 nm with oscillator strengths 0.048 and 0.053, and at 280.6 and 247.7 nm with oscillator strength of 0.070 and 0.067, respectively. In cluster III, there are four longer wavelength absorptions obtained at 276.5, 274.4, 267.0, and 263.5 nm.

In the case of cluster I, the longest wavelength of absorption is obtained by electron transfer from MO-139 to MO-142. These are mainly localized at W233 (Figure 2A) with a minor contribution from a π* orbital located on R234 in MO-142. This implies that the π orbital of residue W233 can be the electron donor orbital and the π* orbitals of residue R234 and W233 the electron acceptors involved in the electron transfer

reaction induced by the UV-B irradiation. The second wavelength absorption at 249.3 nm being slightly larger than at 245.5 nm is obtained by electron transfer from MO-141 to MO-144. The π orbital of residue W285 is in this case the electron donor orbital and the π^* orbitals of residues W285 and W337 the electron acceptors.

In cluster II, the longest wavelength absorption describes an electron transferred from MO-140 to MO-145, again mainly located on W233 (Figure 2B). The π^* orbital of W285 and σ^* orbital of R286 are also involved in MO-145. Upon excitation, the π orbital of W233 will thus be the electron donor orbital, and the π^* orbitals of W233 and W285 and the σ^* orbital of R286 the electron acceptor orbitals. The second wavelength absorption at 247.7 nm is obtained by electron transfer from MO-138 to MO-146, mainly located on the W337 residue.

In cluster III, the first three long wavelength absorptions include the electron transfer from MO-140 to MO-143, from MO-135 to MO-143, and from MO-140 to MO-147. Again, MO-140 is mainly localized to residue W233 (Figure 2C). Contributions from the π^* orbitals of residues W285 and R338 are seen in MO-143, and π orbitals of residues W285 and W337 are involved in MO-135. The third singlet excited state at $\lambda = 267.0$ nm is highly localized to W233. The fourth long wavelength absorption is the electron transfer from MO-136 to MO-144. Both of these are mainly localized to residue W337, but with the π^* orbital of residue W285 and σ^* orbital of R338 also being involved in MO-144.

The first triplet states of the clusters were optimized at the B3LYP/6-31G(d,p) level in gas phase. The optimized structures and their spin density distributions are shown in Figure 3. The electronic and free energies related to the S_0 and T_1 states are listed in Table 2 for each cluster. In the optimized

Table 2. Electronic Energies with and without ZPE Correction and Gibbs Energies of the Clusters in the Ground and First Triplet States[a]

system	state	E_{vacuum}[b]	E_{vacuum} + ZPE	ΔG_{vacuum}^{298}[c]
cluster I	S_0	−1683.26489	−1682.62311	−1682.70604
	T_1	66.4	64.4	62.5
cluster II	S_0	−1683.23531	−1682.64112	−1682.67013
	T_1	47.3	46.4	40.4
cluster III	S_0	−1683.22682	−1682.64163	−1682.66485
	T_1	39.6	38.2	32.9

[a]Absolute energies for the S_0 states (au) and relative energies for the T_1 states (kcal/mol) relative to S_0. [b]Gas-phase optimized structure. [c]$\Delta G_{vacuum}^{298} = E_{vacuum} + \Delta G_{corr}^{298}$.

structures, NBO analysis reveal that each C−N bond in the guanidinium groups of the arginines has an average of 1.99 electrons with 60% N character in $sp^{2.0}$ and 40% C character in

$sp^{2.7}$, indicative of C−N single bonds, whereas the aromatic rings are conserved in the indol groups of the tryptophans. The guanidinium groups of the arginines thus have a pyramidal structure and the hydrogens of the primary amines are out of plane relative to the S_0 state (Figure 3A,C,E). The nonplanarity of the triplet structures is induced by the localization of the unpaired electrons. The spin densities are mainly distributed on residue W233 and the respective arginines (R234, R286, and R338; Figure 3B,D,F). The spin density values are 1.000, 0.991, and 1.015 e$^-$ on residues R234, R286, and R338, respectively, and approximately 1.000 e$^-$ on residue W233. In each cluster, one proton is furthermore transferred spontaneously from residue W233 to D129, with a resulting H---N distance of ∼0.15−0.18 nm. Hence, in the first triplet excited state, protonated D129 residue, deprotonated W233 radicals, and arginyl radicals (R234, R286, and R338) are formed in the three clusters, in agreement with the mechanistic hypotheses outlined in Scheme 2. The Gibbs energy differences between the optimized ground state and the optimized T_1 state in gas phase are 62.5, 40.4, and 32.9 kcal/mol in clusters I, II, and III, respectively.

The single mutant W285F is a constitutive dimer also in the presence of UV-B.[8,11] This suggests that the UV-B-induced monomerization of the UVR8 dimer is critically controlled by residue 285. To better understand the mechanism of monomerization, clusters including residues D129, W233, W285F, W337, and the single arginine (R234, R286, or R338) were also investigated. TD-DFT calculations of the vertical singlet excited states based on the optimized S_0 structures were as before performed at the B3LYP/6-31G-(d,p)//TD-ωB97xd/6-31G(d,p) level in the gas phase. The absorption wavelengths >245.5 nm with oscillator strengths larger than 0.03 are listed in Table 3. The optimized structures and the key orbitals involved in the electronic excitation are shown in Figure 4. NBO analyses reveal that each C−N bond in the guanidinium groups of the arginines have an average of 1.99 electrons with 60% N character in $sp^{1.7}$ and 40% C character in $sp^{2.0}$, similarly to the wild-type cluster. The aromatic character of the tryptophan indol groups are also retained as revealed by the NBO analyses. The D129-W233 hydrogen bond is observed in the each cluster (Figure 4).

For cluster I^{W285F}, the longest wavelength absorptions involves $\pi \rightarrow \pi^*$ electron transfer on residue W233, as shown in Figure 4A. Residues R234, F285, and W337 are no longer electron accepting orbitals at the longer wavelength absorption, which is approximately 8 nm blue-shifted compared to that of the corresponding cluster in the wild-type system. For the longer wavelength absorption (>245.5 nm) of cluster II^{W285F}, the electron is transferred from the π orbital of residue W233, to the π^* orbital of residue W233 and the σ^* orbital of residue R286, as seen in Figure 4B. The π^* orbital of residue

Table 3. Long Absorption Wavelengths (>245.5 nm) and Their Oscillator Strengths (f) in the Clusters Including the W285F Single Mutant

systems[a]	S1/nm (f)	orbital	S2/nm (f)	orbital
cluster I^{W285F}	266.1 (0.054)	130 → 132		
cluster II^{W285F}	284.9 (0.061)	130 → 135		
cluster III^{W285F}	266.3 (0.070)	131 → 136	252.2 (0.040)	126 → 135
		131 → 140		

[a]Cluster I^{W285F} including residues W233, W285F, W337, D129, and R234; Cluster II^{W285F} including residues W233, W285F, W337, D129, and R286; and Cluster III^{W285F} including residues W233, W285F, W337, D129, and R338
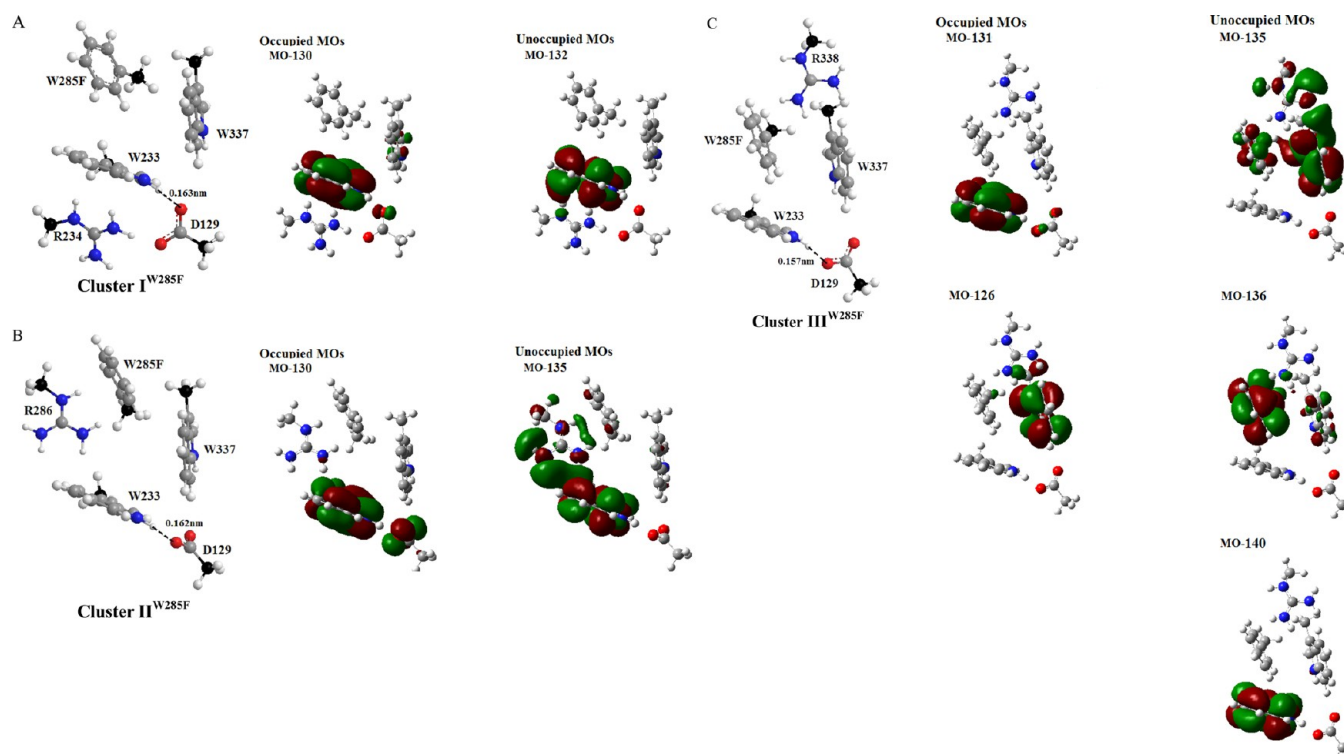
Figure 4. Optimized S_0 structures and the key orbitals for the electron transfer in (A) cluster I^{W285F}, (B) cluster II^{W285F}, and (C) cluster III^{W285F} of the W285F mutant. The images of the optimized structures were produced using ChemDraw12.0, and the molecular orbitals were produced using Gaussview 5.0 with the isovalue = 0.02.

Table 4. UVR8 Mutant Systems and Average Cα RMSD and ΔSASA Values during the Last 30 ns of the MD Simulations

systems	UV-B-induced residues included in the photoreacted UVR8 dimer	Cα-RMSD $\pm$ std dev (nm)^d	ΔSASA (nm^2)^e
WT		0.1589 $\pm$ 0.03	
I	W233dhyd,^{a} Dh129,^{b} and R234rad^c	0.1552 $\pm$ 0.03	0.02
II	W233dhyd, Dh129, and R286rad	0.2374 $\pm$ 0.03	2.71
III	W233dhyd, Dh129, and R338rad	0.2588 $\pm$ 0.04	4.94

^{a}W233dhyd is the deprotonated W233 radical. ^{b}Dh129 is protonated D129. ^{c}R234rad, R286rad, and R338rad are the different neutral arginyl radicals, respectively. ^{d}Average Cα RMSD value with fluctuations ($\pm$SD) of each system during the last 30 ns of the simulations compared to their corresponding starting structures. ^{e}Relative average solvent accessible surface area (ΔSASA) for systems I, II, and III during the last 30 ns of the simulations, compared to values for the wild-type UVR8.

F285 is no longer involved in the W285F mutant (Figure 2B, MO-145). The first wavelength absorption in cluster II^{W285F} is only blue-shifted by 4 nm relative to the wild type. In cluster III^{W285F} containing R338, the longest wavelength absorption involves $\pi \rightarrow \pi^*$ electron transfer from residues W233 to F285, and local excitation on residue W233 similar to that seen in the first and third wavelength absorption in the wild-type system, respectively, but is blue-shifted by 10 nm. R338 is no longer involved in the electron accepting orbitals at the longer wavelength absorptions, compared to the wild-type system. The second wavelength absorption in the W285F mutant is similar to the fourth wavelength absorption in the wild type but is blue-shifted by approximately 10 nm. The excitation involving W285 as electron donor in the wild type is absent in the W285F mutant (Figure 4C). Thus, given the W285F mutation, the longest wavelength absorptions are blue-shifted, compared to those of the wild-type system in clusters I^{W285F} and III^{W285F}. Electron transfer from residue W233 to R234/R338 is impaired, which means that residue W285 is a necessary participant in the electron transfer also in cluster III. However, in cluster II^{W285F}, mutation of residue 285 has only little

influence on the first absorption wavelength and on the electron transfer from residue W233 to R286.

It is thus first concluded that the preferred reaction mechanism in cluster I is a UV-B-induced electron transfer directly from W233 to R234 concomitant with proton transfer from W233 to D129, whereas for clusters II and III the reaction starts with the electron transfer from residue W233 via W285, to the arginine residue (R286 or R338), with a simultaneous proton transfer from W233 to D129. Second, given that the UV-B-induced monomerization is known to be controlled by residue W285, the hypotheses for the mechanisms involving clusters I and III (including R234 and R338, respectively) are, on the basis of the quantum calculations of the W285F mutant systems, more consistent with experiments than a mechanism involving cluster II.

3.2. Evaluating the Mechanistic Hypotheses Using Steered Molecular Dynamics (SMD) Simulations in Whole UVR8 Dimer Protein Systems. To evaluate the reaction mechanism hypothesis, three systems involving whole UVR8 protein dimers (containing 10 000 protein atoms) were investigated after absorption of UV-B, as listed in Table 4. The
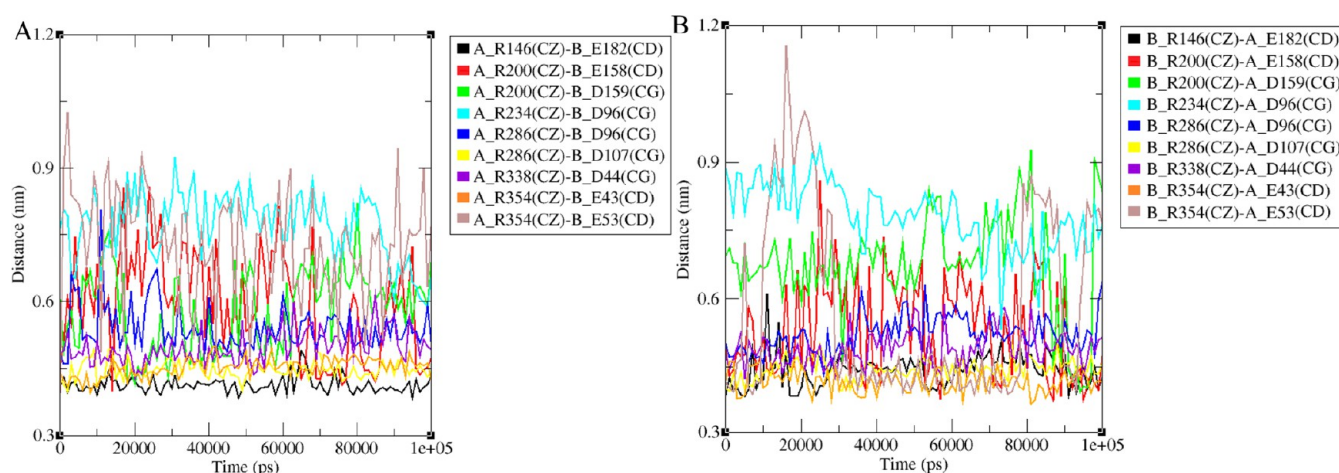
Figure 5. (A) Distances between CZ atoms in monomer A and atom types CD/CG in monomer B of the wild-type UVR8 dimer. (B) Distances between CZ atoms in monomer B and atom types CD/CG in monomer A of the wild-type UVR8 dimer.

dissociation of the wild-type UVR8 dimer and its mutants is a dynamic process, but studies of the behavior of a UVR8 system upon complete dissociation need to be followed during a longer period of time than what is used in conventional MD simulations. Therefore, SMD simulations,[52] based on the refined structures after 100 ns MD simulations, were employed. The images of the starting structures used in the pulling simulations are shown in the Supporting Information, Figure S1. α-Carbon root-mean-squared deviation (Cα-RMSD) values and differences in average solvent accessible surface area (ΔSASA) for each system prior to SMD are listed in Table 4. The values represent averages calculated over the last 30 ns of the simulations. The SASA averages were calculated using the YASARA software.[53]

3.2.1. Stability of Unreacted UVR8 Dimer. In the crystal structure, the acidic (aspartic acid/glutamic acid) and basic arginine surface patches of one UVR8 monomer interact with the other UVR8 monomer's basic and acidic surface patches, respectively, by intermonomeric hydrogen bonds to form a symmetric homodimer. The distances of the formed salt bridges were measured between atom type CZ (the central carbon of the arginine guanidinium group) and atom type CD/CG representing the carbons of the carboxylate groups of the glutamic/aspartic acids of the respective monomers at the interface (Supporting Information Figure S2). The distances for the double hydrogen-bonded salt bridges are approximately 0.4 nm for R146(CZ)-E182(CD) and R286(CZ)-D107(CG) and ∼0.47 nm for the single hydrogen-bonded salt bridges R200(CZ)-E158(CD), R286(CZ)-D96(CD), R338(CZ)-D44(CG), and R354(CZ)-E43/E53(CD). During the 100 ns simulations, the interface of the wild-type UVR8 dimer shows a maintained integrity of the hydrophobic core. The average Cα-RMSD value during the last 30 ns of the simulation is 0.159 nm. The distances show relatively small fluctuations for all the salt bridges found in the crystal structure, which indicates their high stability. The only exceptions are seen for R200(CZ)-E158(CD) and R354(CZ)-E53(CD) (Figure 5A,B) for which the distances fluctuate dramatically. This is indicative of weak salt bridge interactions between these residues. The distances between R200(CZ) and D159(CG) are ∼0.68 nm in the crystal structure but vary significantly along the MD simulations, similar to the salt bridge R354-E53. A weak salt bridge is thus

formed and interrupted throughout the MD simulation, due to the close spatial location of the amino acid side chains.

3.2.2. Effect of the Photochemical Reaction on UVR8 Dimer Stability. In system I, the average Cα-RMSD value is approximately 0.155 nm during the last 30 ns of the simulation, similar to that for the UVR8 dimer before the photochemical reaction. Furthermore, during the MD simulation, the fluctuation distances for all the salt bridges are similar to those in the unreacted UVR8 dimer (Figure 6A,B). We can thus conclude that the photochemical reaction as described for system I will not destabilize the UVR8 dimeric structure.

For a UVR8 dimer reacting according to the R286 radical model system II, the average Cα-RMSD value is approximately 0.237 nm during the last 30 ns of the MD simulations. This is relatively large, compared to the value for the UVR8 dimer before absorption of UV-B. The distances of the salt bridges between residues R146 and E182, and between residues R354 and E43 are stable during the simulations, as shown in Figure 6C,D, whereas the distance between R146 of UVR8 monomer A (R146^A) and E182 of UVR8 monomer B (E182^B) increases to 0.5 nm toward the end of the simulation, leading to the disruption of this hydrogen-bonded salt bridge in the last snapshot. Furthermore, the distances between residues R286 and D96 increase and fluctuate dramatically, compared with the situation prior to UV absorption, resulting in the interruption of the single hydrogen-bonded salt bridge R286-D96 in the last snapshot (Figure S1, Supporting Information). On the other hand, the distances of R234^A-D96^B are approximately 0.4 nm in the intervals 35−70 and 90−100 ns of the simulation, and around 0.4 nm for R234^B-D96^A after 5 ns of the simulation, leading to double hydrogen-bonding of these salt bridges in the last snapshot. The formation of salt bridges R234-D96 are not found in wild-type UVR8 and in systems I and III. When comparing parts C and D of Figure 6, we note that the distance fluctuations for several of the salt bridges differ between the two monomers. The distance between residue R286^A and D107^B is approximately 0.6 nm during the first 30 ns, decreases to ∼0.4 nm in the 30−70 ns interval, and again increases to ∼0.6 nm during the last 30 ns of the simulation. On the other hand, the distance for the corresponding R286^B-D107^A salt bridge counterpart is about 0.45 nm during the first 45 ns of the simulation with small fluctuations (similarly to the system before UV-B absorption), then increases to ∼0.5 nm during the
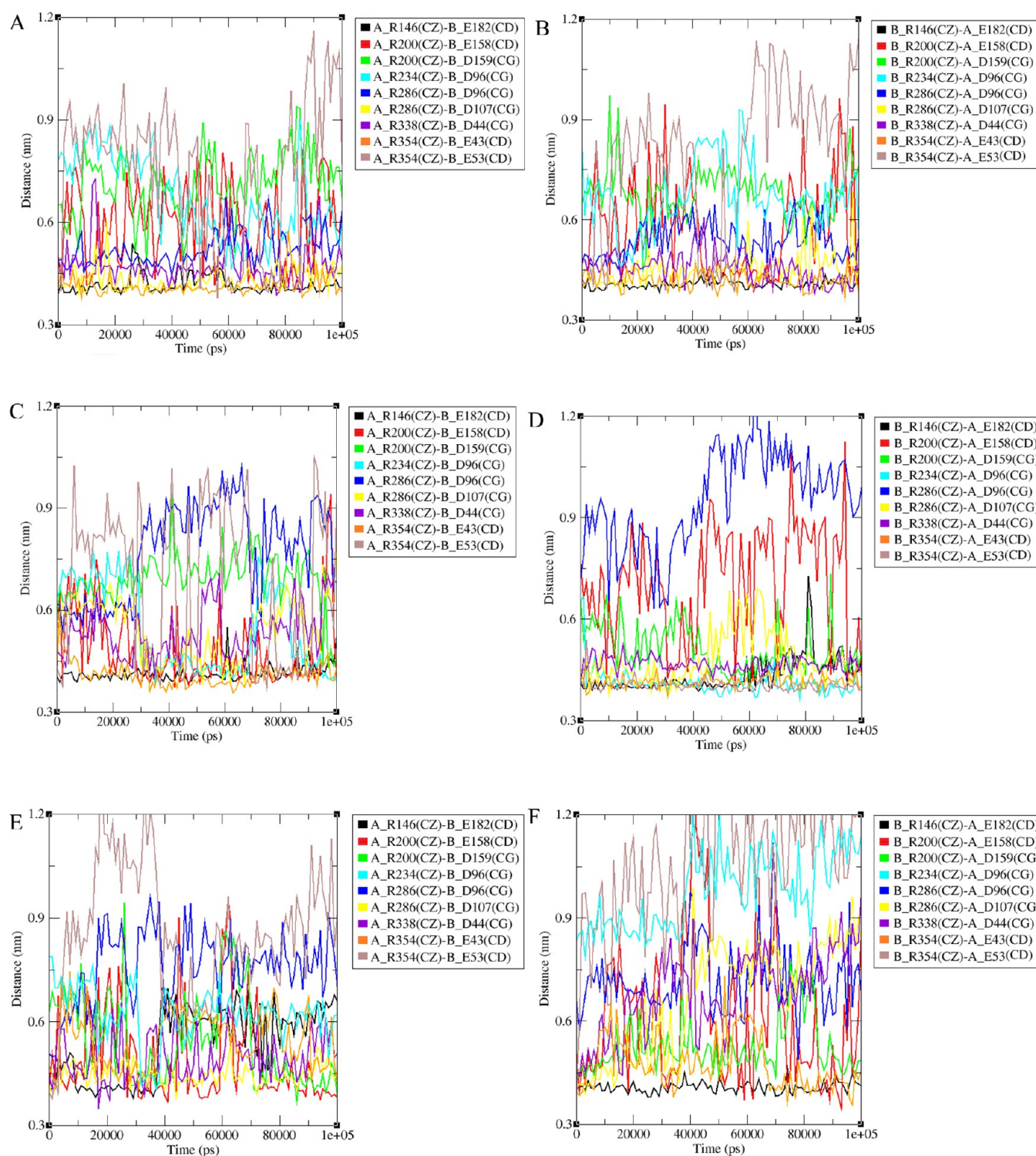
Figure 6. (A) Distances between atom types CZ in monomer A and atom types CD/CG in monomer B of system I. (B) Distances between atom types CZ in monomer B and atom types CD/CG in monomer A in system I. (C) Same as in (A) but for system II. (D) Same as in (B) but for system II. (E) Same as in (A) but for system III. (F) Same as in (B) but for system III. Atom types CZ and CD/CG represent the carbons of the guanidinium group of arginine and the carboxylate group of glutamic acid/aspartic acid, respectively, as defined in the Supporting Information Figure S2.

45−70 ns interval, and finally stabilizes at ∼0.45 nm during the last 30 ns of the simulation, with the formation of a single hydrogen-bonded interaction in the last snapshot. Between residues R200[A] and E158[B], and between residues R200[B] and D159[A], short distances with relatively small fluctuations were obtained after 40 ns simulation time. On the other hand, the distances of the R200[B]-E158[A] and R200[A]-D159[B] counterparts display large and dramatic fluctuations throughout the MD simulations. Finally, the salt bridge pairs R338[B]-D44[A] and R354[B]-E53[A] fluctuate to a slightly smaller extent during the simulation, compared to their respective R338[A]-D44[B] and R354[A]-E53[B] counterparts.

For the UVR8 dimer reacting to UV-B absorption according to the system III mechanism (containing the R338 radical), the average Cα-RMSD value is 0.259 nm during the last 30 ns simulations, i.e., even larger than for system II. From Figure 6E,F, we see that the distances between R200-D159, R286-D96, R338-D44, and R354-E43 fluctuate significantly compared to the situation before UV-B absorption. Only the distances between residue pairs R286[A]-D107[B], R200[A]-E158[B], and R146[B]-E182[A] fluctuate relatively little throughout these MD simulations, leading to the presence of a single hydrogen-bonded salt bridge R286[A]-D107[B] and two double hydrogen-bonded salt bridges (R200[A]-E158[B] and R146[B]-E182[A]) in the last snapshot from the simulation (Supporting Information Figure S1). The large fluctuations arise from the formation and breakage of the intermonomeric hydrogen bonds during the MD simulation. This shows that the dimeric structure according to the system III mechanism is destabilized, compared to the dimer prior to the absorption of UV-B. The larger fluctuations obtained in system III, compared to system II, indicate that R338 is more important for the dimer stability than R286.

Compared to the situation for the wild-type UVR8 dimer before UV-B absorption, in systems II and III the average ΔSASAs increase over the course of the 100 ns MD trajectories, although momomers A and B do not completely dissociate from the core of the structure in either of these systems. The increased solvation of the dimer interface leads to destabilization of the dimeric structures, and it is possible that substantially longer simulation times would lead to dissociation. The average ΔSASA of system I, on the other hand, is similar to that for the UVR8 dimer before the photochemical reaction, again indicating a smaller influence on the interaction at the dimer interface for this photochemical pathway.

3.2.3. Steered MD Simulations. To explore the stabilities of the dimeric systems after the photochemical reaction, steered MD simulations were performed, in which monomer B was gradually pulled away from the position-constrained monomer A. The change in interaction energy between the two monomers was assessed for each system during the dissociation process, as shown in Figure 7. Electrostatic and van der Waals (vdW) interactions predominantly contribute to the total
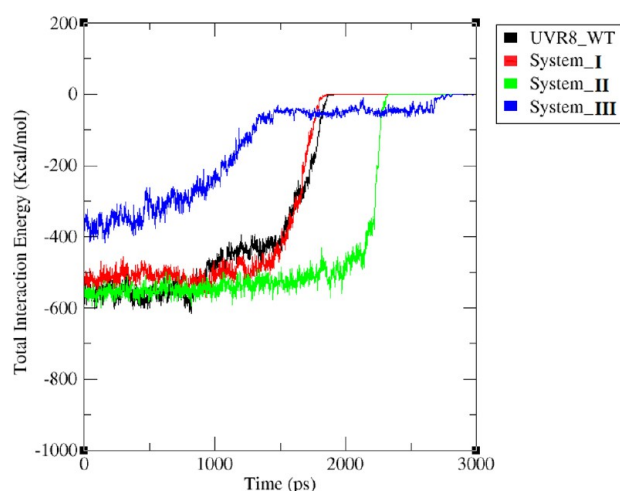
interaction of each system. During the course of the pulling simulation, monomer B gradually shifts away from monomer A and the total interaction energies vanish. At the starting point, the interaction energy of the wild-type UVR8 dimer and system I is ∼550 kcal/mol and is only slightly weaker (∼530 kcal/mol) in system II. In the interval between 1300 and 1800 ps of the simulation, the energy curves quickly go to 0 for the wild-type UVR8 and system I: The corresponding dissociation interval for system II is at 2100−2300 ps. System III displays the weakest interaction energy (∼360 kcal/mol) at the starting point, which rapidly weakens to 60 kcal/mol between 1300 and 2500 ps and gradually reaches 0 at around 2700 ps of the simulation.

Salt bridges are an abundant type of noncovalent interactions and are vital in stabilizing the UVR8 dimeric structure. The key interface salt bridges in the wild-type UVR8 dimer before absorption of UV-B are R146-E182, R200-E158/D159, R286-D107/D96, R338-D44, and R354-E43/E53. The presence of these salt bridges during the dissociation processes are presented in Figure 8A. The cutoff radius of a salt bridge is defined to be 0.35 nm between the heavy atoms (N and O). It can be seen that salt bridges from residues R146, R246, R338, and R354 are stable during the SMD simulations until dissociation starts taking place in the interval 1600−1900 ps.

The salt bridges present during the corresponding pulling process of systems I, II, and III are displayed in Figure 8B−D. In system I, the key interface salt bridges R146-E182, R286-D107, R338-D44, and R354-E43 are conserved and stable, similar to the case for the dimer before UV-B absorption. Only the relatively weak single hydrogen-bonded salt bridges R200[A]-E158[B], R200-D159, and R354-E53 are missing. These findings support the conclusion that the residues in system I have very little influence on the stability of the dimeric structure after UV-B absorption.

In system II, the double hydrogen-bonded salt bridges R234[A]-D96[B], R354[A]-E43[B], and R354[B]-E53[A], and the single hydrogen-bonded salt bridges between residues R146, R200, R234, and R338 and R354 in monomer B and residues E182, E158, D96, D44, and E43 in monomer A, respectively, are the most long lasting salt bridges found during the pulling process, as shown in Figure 8C. The strong interactions between arginines in monomer B and glutamic acids/aspartic acids in monomer A correspond to the relatively short distances and small fluctuations between these residues obtained in the 100 ns MD simulations but are not seen for their respective A/B counterparts, as shown in Figure 6C,D. The strong interface interaction of system II, which is similar to the UVR8 dimer before UV-B absorption, as shown in Figure 7, is attributed to the several strong hydrogen-bonded salt bridge interactions conserved and the additional salt bridge (i.e., R234-D96) formed between the monomers. No salt bridges prevail after 2350 ps.

In system III, the interactions of the key interface salt bridges are weakened considerably, except for the single hydrogen-bonded salt bridge between R146[B]-E182[A], which is relatively stable until 1250 ps of the simulation. After 1250 ps, all the key interface salt bridges are interrupted except for salt bridge R200[A]-E158[B] that is present until the monomers are completely dissociated. This explains that the binding interaction energy of system III rapidly drops to 60 kcal/mol in the interval 1500−2500 ps, as shown in Figure 8D. No salt bridges are present after 2650 ps.
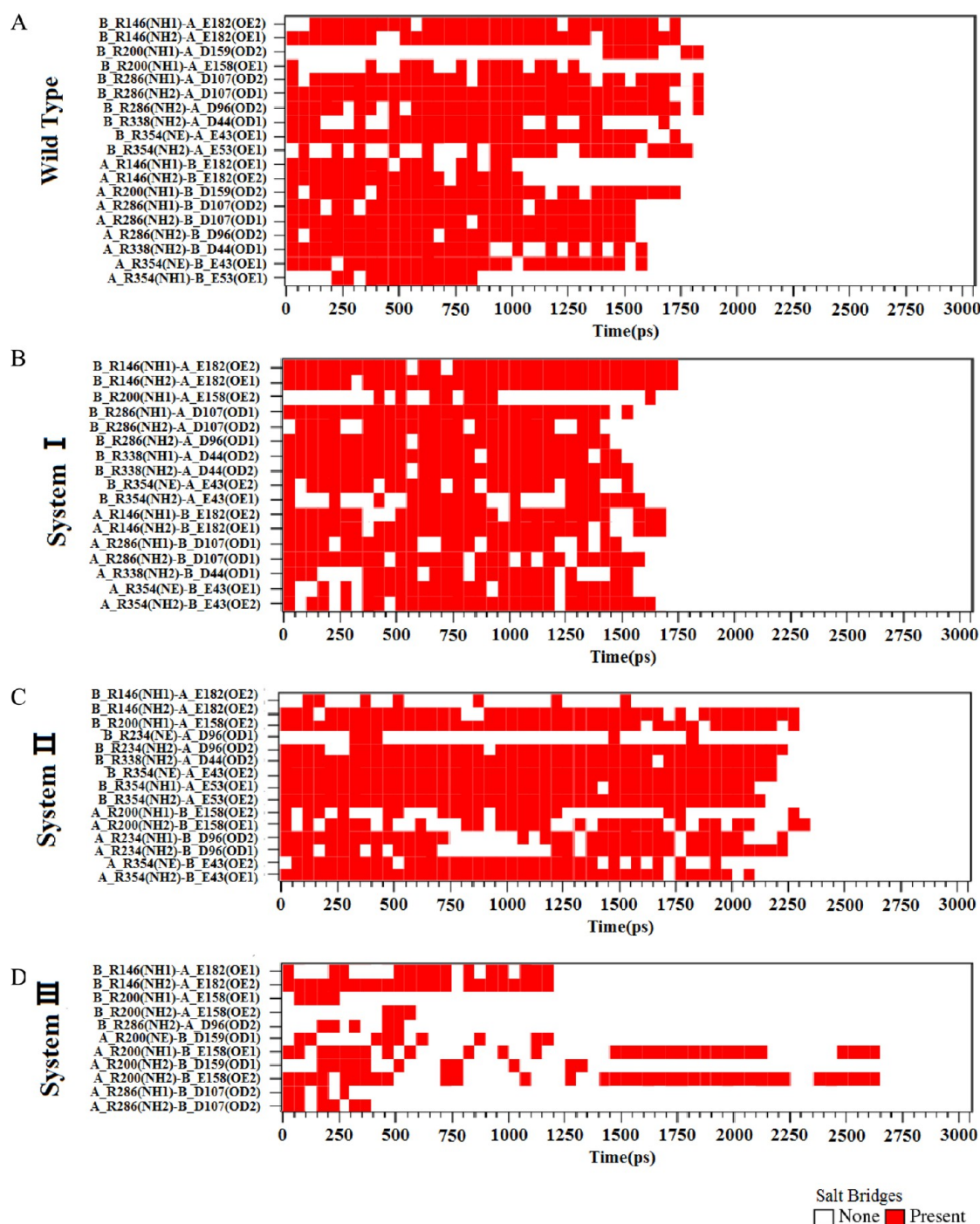

Figure 7. Total interaction energies at the interface of the UVR8 dimers before and after the UV-B-induced photochemical pathways I, II, and III during the SMD simulations.

Figure 8. Presence of salt bridges between the different amino acid residues in monomers A and B, respectively in (A) wild-type UVR8 before the photoreaction, (B) UVR8 dimer system I, (C) UVR8 dimer system II, and (D) UVR8 dimer system III. Atom types NH1(2) and NE represent the nitrogen atoms from the primary and secondary amine groups in arginine, respectively, and atom types OD1(2) and OE1(2) are the oxygen atoms from the carboxylate groups in aspartic acid and glutamic acid, respectively, as defined in the Supporting Information Figure S2.

3.3. Binding Energy Cutoff for UVR8 Dimer Monomerization. To determine the UVR8 monomerization threshold, a novel ROC curve approach was employed. Sensitivity and specificity are the main features allowing the design of the ROC curve. A preliminary indication about the quality of the model can be obtained by visual inspection of the plot, especially in the left region (Figure 9) where relevant enrichments take place. The area under the ROC curve (AUC) is an important indicator of the model's performance and is independent of the selected cutoff values. Seven single mutants, three double

mutants, and the wild-type UVR8 dimer were investigated to determine the binding energy threshold of UVR8 dimer monomerization by running SMD simulations on the structures obtained after 100 ns MD refinement. Interaction energies as function of the simulation time for all the mutants are shown in the Supporting Information, Figure S3. The reported structures of these mutants[8,11] and the $\Delta\Delta E_{bind}$ calculated using the theoretical methods are listed in Table 5. The single-mutant structures of UVR8 from ref 11 and the double-mutant structures from ref 8 were used in the ROC curve
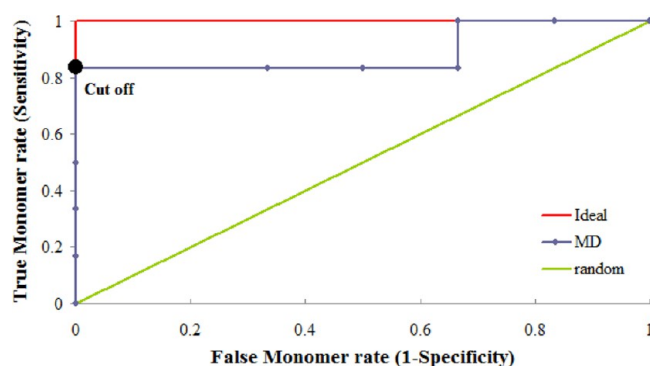
Figure 9. ROC curve obtained from eqs 1 and 2 through all possible score thresholds, based on the experimentally determined structures of wild-type, single-mutant, and double-mutant UVR8 dimers (R286A assumed monomeric).

Table 5. Quaternary Structures of Mutants Obtained from Experiments and $\Delta\Delta E_{bind}$ Calculated by Using the Theoretical Methods

system	quaternary structure[exp]	$\Delta\Delta E_{bind}$ (kcal/mol)
WT	dimer[8,11]	
R146A	dimer[11]	136.8
R200A	dimer[11]	72.9
W285A	monomer[11]	147.7
W285F	dimer[11]	99.0
R286A	dimer[8]/monomer[11]	47.7
W337F	dimer[11]	24.6
R338A	monomer[11]	189.5
D96N/D107N	monomer[8]	152.8
R146A/R286A	monomer[8]	297.0
R286A/R338A	monomer[8]	313.6
system I	dimer (this work)	33.1
system II	dimer (this work)	10.9
system III	monomer (this work)	189.2

determination. $\Delta\Delta E_{bind}$ is the average of the reduction in binding energy of the mutants compared to that for the wild-type UVR8 dimer, as computed from the first 500 ps of the SMD simulations, before the dissociation of the two monomers. For a given value of the monomerization energy cutoff, the selectivity and specificity was computed according to eqs 1 and 2, and a point on the ROC curve was added. The final ROC curve is shown in Figure 9. The AUC value of 0.889 is indicative of a very good predictability and the cutoff value of $\Delta\Delta E_{bind}$ is 140 kcal/mol with the highest ACC of 91.7% and MCC of 0.845 (employing eqs 3 and 4). This means that a monomeric structure of UVR8 is obtained when the reduction in dimer binding energy is larger than 140 kcal/mol. One consistent outlier is seen in the R286A mutant. The $\Delta\Delta E_{bind}$ for this mutant is about 48 kcal/mol, suggesting a dimeric structure. A monomeric structure of this mutant was observed in ref 11 whereas a dimeric structure was found experimentally in ref 8. Using the result from ref 8 instead of that of ref 11 (which gave the above result), and thus considering R286A to be a dimer, an ideal ROC curve would be obtained. In this case the ACC is 100% and MCC 1.000. $\Delta\Delta E_{bind}$ remains unaltered at 140 kcal/mol.

In the presence of UV-B radiation, a constitutive monomer form of UVR8[W285A] is apparent as described in refs 11, 15, and 27. In contrast, in ref 8, purified UVR8[W285A] was determined to be a dimer. In our work, we find a $\Delta\Delta E_{bind}$ of UVR8[W285A] of

approximately 148 kcal/mol, close to the cutoff of 140 kcal/mol, indicating that both monomer and dimer structures of UVR8[W285A] can coexist experimentally. In the photoreacted systems I and II, the $\Delta\Delta E_{bind}$ is 33.1 and 10.9 kcal/mol, respectively, leading to conservation of the dimeric structures. However, in system III, the $\Delta\Delta E_{bind}$ is approximately 189.2 kcal/mol, and thus a monomeric structure is predicted for this system.

4. CONCLUSIONS

Possible reaction mechanisms for UV-B-induced UVR8 monomerization was investigated using quantum chemical cluster calculations. Clusters including residues D129, W233, W285/W285F, and W337, together with single arginines R234, R286, or R338, were studied to unveil the roles played by the respective arginines and their interactions with the key UV-absorbing tryptophans. In the cluster including R234, an electron was found to be transferred directly from W233 to R234 with a simultaneous proton transfer from W233 to D129. For the R286- or R338-containing clusters, the suggested mechanisms include an electron transfer induced by UV-B irradiation from residue W233 to intermediate residue W285, followed by onward transfer to the arginine concomitant with a proton transfer from W233 to D129. Experimentally, it was found that the dimeric structure of mutant UVR8[W285F] is a constitutive dimer in the presence of UV-B,[8,11] implying that the UV-B-induced monomerization reaction is impaired by the W285F mutation. To test this, cluster calculations were also performed on the same clusters but including the W285F mutant. In the R234- and R338-containing clusters, the hypothetical reactions were interrupted after W285F mutation. However, in the R286-containing cluster, no influence of the mutation was seen on the electron transfer between residues W233 and R286. It is thus concluded that the mechanisms of cluster I and III, involving either R234 or R338, are more consistent with the experimental data than a mechanism as described by cluster II.

To further evaluate the photochemical reaction mechanism, explicit solvent MD and SMD simulations were employed to analyze the interaction between the monomers of the wild-type UVR8 dimer before UV-B absorption and the three systems after photochemical reaction has taken place, to investigate the effects of the different mechanisms on the monomerization of the UVR8 dimer by UV-B irradiation. Protonated D129, deprotonated W233 radical, and R234/R286/R338 radical modifications were represented in the systems I/II/III. Solvent accessible surface area (SASA) analyses indicate that the dimeric interfaces of systems II and III are more solvent-exposed than the wild-type dimer before UV-B absorption, whereas the average SASA of system I obtained during the last 30 ns of the MD simulation was similar to that of the wild-type dimer. From the salt bridge analyses, the number of primary salt bridges was found to dramatically decrease in system III, but only slightly in system II, whereas the number was essentially unaltered in system I, compared with the case of the UVR8 dimer before UV-B absorption. Furthermore, the binding energy reductions ($\Delta\Delta E_{bind}$) of systems I, II, and III were 33.1, 10.9, and 189.2 kcal/mol, respectively, relative to the wild-type dimer. This suggests that after the photochemical reaction has taken place, the system III dimeric structure is destabilized more than a corresponding system II dimer. The modifications introduced in system I have less influence on the stability of the UVR8 dimeric structure.

A novel application of ROC curves based on data for seven single mutants, three double mutants, and the wild-type UVR8 dimer was introduced, leading to a reliable $\Delta\Delta E_{bind}$ cutoff for the determination of a monomeric structure. The 140 kcal/mol cutoff value of $\Delta\Delta E_{bind}$ was obtained as having the highest ACC of 91.7% and MCC of 0.845, assuming the R286A mutant to be monomeric. Applying this cutoff value to our photoreaction models, it is thus concluded that a monomeric structure is obtained only for system III containing protonated D129, deprotonated W233 radical and neutral R338 radical forms. The preferred mechanism for UV-B-induced UVR8 monomerization, as inferred from this work, thus involves an electron transfer from residue W233 to W285 and onward to R338, coupled to simultaneous proton transfer from W233 to D129 (the cluster III model). Due to the formation of a neutral R338 radical, salt bridges containing the R338 residue were disrupted together with a number of other key salt bridges and only three important salt bridges were conserved toward the end of 100 ns MD simulations, too few to hold the UVR8 dimer together.

ASSOCIATED CONTENT

S Supporting Information

The structures of the UVR8 dimer and systems I, II, and III during the MD simulations (Figure S1). Atom type labels for N, O, and C atoms in arginine, aspartic acid, and glutamic acid (Figure S2). The total interaction energies of the wild-type UVR8 dimer and its mutants R146A, R200A, W285A, W285F, R286A, W337A, R338A, D96N/D107N, R146A/R286A, and R338A/R286A, during the SMD simulations (Figure S3). Cα-RMSDs of the wild-type UVR8 dimer and its mutants during the 100 ns MD simulations (Figure S4). This material is available free of charge via the Internet at http://pubs.acs.org.

AUTHOR INFORMATION

Corresponding Author
*L. Eriksson: e-mail, leif.eriksson@chem.gu.se.

Notes
The authors declare no competing financial interest.

ACKNOWLEDGMENTS

REFERENCES

(1) Bornman, J. F. Target Sites of UV-B Radiation in Photosynthesis of Higher Plants. *J. Photochem. Photobiol. B: Biol.* **1989**, *4*, 145–158.

(2) Strid, Å.; Chow, W. S.; Anderson, J. M. UV-B Damage and Protection at the Molecular Level in Plants. *Photosynth. Res.* **1994**, *39*, 475–489.

(3) Wu, M.; Xu, Q.; Strid, Å.; Martell, J. M.; Eriksson, L. A. Theoretical Study of Pyridoxine (Vitamin B6) Photolysis. *J. Phys. Chem. A* **2011**, *115*, 13556–13563.

(4) Ehling-Schulz, M.; Bilger, W.; Scherer, S. UV-B-Induced Synthesis of Photoprotective Pigments and Extracellular Polysaccharides in the Terrestrial Cyanobacterium Nostoc Commune. *J. Bacteriol.* **1997**, *179*, 1940–5.

(5) Hideg, É.; Jansen, M. A. K.; Strid, Å. UV-B Exposure, ROS and Stress: Inseparable Companions or Loosely Linked Associates? *Trends Plant Sci.* **2012**, *18*, 107–115.

(6) Jansen, M. A. K.; Coffey, A. M.; Prinsen, E. UV-B Induced Morphogenesis: Four Players or a Quartet? *Plant Signaling and Behavior 7* **2012**, *7*, 1185–1187.

(7) Brown, B. A.; Cloix, C.; Jiang, G. H.; Kaiserli, E.; Herzyk, P.; Kliebenstein, D. J.; Jenkins, G. I. A UV-B-Specific Signaling Component Orchestrates Plant UV Protection. *Proc. Natl. Acad. Sci. U. S. A.* **2005**, *102*, 18225–18230.

(8) Christie, J. M.; Arvai, A. S.; Baxter, K. J.; Heilmann, M.; Pratt, A. J.; O'Hara, A.; Kelly, S. M.; Hothorn, M.; Smith, B. O.; Hitomi, K.; et al. Plant UVR8 Photoreceptor Senses UV-B by Tryptophan-Mediated Disruption of Cross-Dimer Salt Bridges. *Science* **2012**, *335*, 1492–1496.

(9) Heijde, M.; Ulm, R. UV-B Photoreceptor-Mediated Signalling in Plants. *Trends Plant Sci.* **2012**, *17*, 230–237.

(10) Jenkins, G. I. Signal Transduction in Responses to UV-B Radiation. *Annu. Rev. Plant Biol.* **2009**, *60*, 407–31.

(11) Wu, D.; Hu, Q.; Yan, Z.; Chen, W.; Yan, C.; Huang, X.; Zhang, J.; Yang, P.; Deng, H.; Wang, J.; et al. Structural Basis of Ultraviolet-B Perception by UVR8. *Nature* **2012**, *484*, 214–219.

(12) Brown, B. A.; Jenkins, G. I. UV-B Signaling Pathways with Different Fluence-Rate Response Profiles are Distinguished in Mature Arabidopsis Leaf Tissue by Requirement for UVR8, HY5, and HYH. *Plant Physiol.* **2008**, *146*, 576–588.

(13) Favory, J. J.; Stec, A.; Gruber, H.; Rizzini, L.; Oravecz, A.; Funk, M.; Albert, A.; Cloix, C.; Jenkins, G. I.; Oakeley, E. J.; et al. Interaction of COP1 and UVR8 Regulates UV-B-Induced Photomorphogenesis and Stress Acclimation in Arabidopsis. *EMBO J.* **2009**, *28*, 591–601.

(14) Kaiserli, E.; Jenkins, G. I. UV-B Promotes Rapid Nuclear Translocation of the Arabidopsis UV-B Specific Signaling Component UVR8 and Activates its Function in the Nucleus. *Plant Cell* **2007**, *19*, 2662–2673.

(15) Rizzini, L.; Favory, J. J.; Cloix, C.; Faggionato, D.; O'Hara, A.; Kaiserli, E.; Baumeister, R.; Schäfer, E.; Nagy, F.; Jenkins, G. I.; et al. Perception of UV-B by the Arabidopsis UVR8 Protein. *Science* **2011**, *332*, 103–106.

(16) Brown, B. A.; Headland, L. R.; Jenkins, G. I. UV-B Action Spectrum for UVR8-Mediated HY5 Transcript Accumulation in Arabidopsis. *Photochem. Photobiol.* **2009**, *85*, 1147–1155.

(17) Heilmann, M.; Jenkins, G. I. Rapid Reversion from Monomer to Dimer Regenerates the Ultraviolet-B Photoreceptor UV RESIST-ANCE LOCUS8 in Intact Arabidopsis Plants. *Plant Physiol.* **2013**, *161*, 547–55.

(18) Wu, M.; Grahn, E.; Eriksson, L. A.; Strid, Å. Computational Evidence for the Role of *Arabidopsis Thaliana* UVR8 as UV-B Photoreceptor and Identificantion of its Chromophore Amino Acids. *J. Chem. Inf. Model* **2011**, *51*, 1287–1285.

(19) Aubert, C.; Vos, M. H.; Mathis, P.; Eker, A. P.; Brettel, K. Intraprotein Radical Transfer During Photoactivation of DNA Photolyase. *Nature* **2000**, *405*, 586–590.

(20) Stubbe, J.; Nocera, D. G.; Yee, C. S.; Chang, M. C. Radical Initiation in the Class I Ribonucleotide Reductase: Long-Range Proton-Coupled Electron Transfer? *Chem. Rev.* **2003**, *103*, 2167–2201.

(21) Shafaat, H. S.; Leigh, B. S.; Tauber, M. J.; Kim, J. E. Resonance Raman Characterization of a Stable Tryptophan Radical in an Azurin Mutant. *J. Phys. Chem. B* **2009**, *113*, 382–388.

(22) Kaiserli, E.; Jenkins, G. I. UV-B Promotes Rapid Nuclear Translocation of the Arabidopsis UV-B Specific Signaling Component UVR8 and Activates its Function in the Nucleus. *Plant Cell* **2007**, *19*, 2662–2673.

(23) Cloix, C.; Kaiserli, E.; Heilmann, M.; Baxter, K. J.; Brown, B. A.; O'Hara, A.; Smith, B. O.; Christie, J. M.; Jenkins, G. I. C-Terminal Region of the UV-B Photoreceptor UVR8 Initiates Singaling Through Interaction with the COP1 Protein. *Pro. Natl. Acad. Sci. U. S. A.* **2012**, *109*, 16366–16370.

(24) Yi, C.; Deng, X. W. COP1 - from Plant Photomorphogenesis to Mammalian Tumorigenesis. *Trends Cell Biol.* **2005**, *15*, 618−625.

(25) Oravecz, A.; Baumann, A.; Máté, Z.; Brzezinska, A.; Molinier, J.; Oakeley, E. J.; Adám, E.; Schäfer, E.; Nagy, F.; Ulm, R. Constitutively Photomorphogenic1 Is Required for the UV-B Response in Arabidopsis. *Plant Cell* **2006**, *18*, 1975−1990.

(26) Wu, M.; Eriksson, L. A.; Strid, Å. Theoretical Prediction of the Protein−Protein Interaction between Arabidopsis Thaliana COP1 and UVR8. *Theor. Chem. Acc.* **2013**, *132*, 11.

(27) O'Hara, A.; Jenkins, G. I. In Vivo Function of Tryptophans in the *Arabidopsis* UV-B Photoreceptor UVR8. *Plant Cell* **2012**, *24*, 3755−3766.

(28) Wu, M.; Strid, Å.; Eriksson, L. A. Interactions and Stabilities of the UV RESISTANCE LOCUS8 (UVR8) Protein Dimer and its key Mutants. *J. Chem. Inf. Model* **2013**, *53*, 1736−1746.

(29) *Molecular Operating Enviroment*, version 2011.10; Chemical Computing Group Inc.: Montreal, Canada, 2011.

(30) Becke, A. D. Density-Functional Thermochemistry. III. The Role of Exact Exchange. *J. Chem. Phys.* **1993**, *98*, 5648−5652.

(31) Stephens, P. J.; Devlin, F. J.; Chabalowski, C. F.; Frisch, M. J. *Ab Initio* Calculations of Vibrational Absorption and Circular Dichroism Spectra using Density Functional Force Fields. *J. Chem. Phys.* **1994**, *98*, 11623−11627.

(32) Liao, R. Z.; Yu, J. G.; Himo, F. Mechanism of Tungsten-Dependent Acetylene Hydratase from Quantum Chemical Calculations. *Proc. Natl. Acad. Sci. U. S. A.* **2010**, *107*, 22523−22527.

(33) Chai, J. D.; Head-Gordon, M. Long-Range Corrected Hybrid Density Functionals with Damped Atom-Atom Dispersion Corrections. *Phys. Chem. Chem. Phys.* **2008**, *10*, 6615−6620.

(34) Chai, J. D.; Head-Gordon, M. Systematic Optimization of Long-Range Corrected Hybrid Density Functionals. *J. Chem. Phys.* **2008**, *128*, 084106.

(35) Tian, B. X.; Eriksson, E. S. E.; Eriksson, L. A. Can Range-Separated and Hybrid DFT Functionals Predict Low-Lying Excitations? A Tookad Case Study. *J. Chem. Theory Comput.* **2010**, *6*, 2086−2094.

(36) Frisch, M. J.; Trucks, G. W.; Schlegel, H. B.; Scuseria, G. E.; Robb, M. A.; Cheeseman, J. R.; Scalmani, G.; Barone, V.; Mennucci, B.; Petersson, G. A.; et al. *Gaussian 09*, v. B.02; Gaussian, Inc.: Pittsburgh, PA, 2009.

(37) Foster, J. P.; Weinhold, F. Natural Hybrid Orbitals. *J. Am. Chem. Soc.* **1980**, *102*, 7211−7218.

(38) Hess, B.; Kutzner, C.; Van der Spoel, D.; Lindahl, E. Gromacs 4: Algorithms for Highly Efficient, Load-Balanced, and Scalable Molecular Simulation. *J. Chem. Theory Comput.* **2008**, *4*, 435−447.

(39) *GROMACS.* http//www. gromacs.org/ (accessed date May 27 2013),

(40) Duan, Y.; Wu, C.; Chowdhury, S.; Lee, M. C.; Xiong, G.; Zhang, W.; Yang, R.; Cieplak, P.; Luo, R.; Lee, T.; et al. Point-Charge Force Field for Molecular Mechanics Simulations of Proteins Based on Condensed-Phase Quantum Mechanical Calculations. *J. Comput. Chem.* **2003**, *24*, 1999−2012.

(41) Case, D. A.; Darden, T. A.; Cheatham, T. E.; Simmerling, C. L.; Wang, J. R.; Duke, E.; Luo, R.; Walker, R. C.; Zhang, W.; Merz, K. M.; et al. *AMBER 12*; University of California: San Francisco, 2012.

(42) Wu, M.; Eriksson, L. A.; Strid, Å. Development of Nonstandard Arginine Residue Parameters for Use with the Amber Force Field. *Chem. Phys. Lett.* **2013**, *584*, 188−194.

(43) Darden, T.; York, D.; Pedersen, L. Particle Mesh Ewald: An N-log(N) Method for Ewald Sums in Large Systems. *J. Chem. Phys.* **1993**, *98*, 10089−10092.

(44) Essmann, U.; Perera, L.; Berkowitz, M. L.; Darden, T.; Lee, H.; Pedersen, L. G. A Smooth Particle Mesh Ewald Method. *J. Chem. Phys.* **1995**, *103*, 8577−8593.

(45) Berendsen, H. J. C.; Postma, J. P. M.; van Gunsteren, W. F.; DiNola, A.; Haak, J. R. Molecular Dynamics with Coupling to an External Bath. *J. Chem. Phys.* **1984**, *81*, 3684−3690.

(46) Hoover, W. G. Canonical Dynamics: Equilibrium Phase-Space Distributions. *Phys. Rev. A* **1985**, *31*, 1695−1697.

(47) Nosé, S. J. A Unified Formulation of the Constant Temperature Molecular Dynamics Methods. *J. Chem. Phys.* **1984**, *81*, 511−519.

(48) Nosé, S.; Klein, M. L. A Study of Solid and Liquid Carbon Tetrafluoride using the Constant Pressure Molecular Dynamics Technique. *J. Chem. Phys.* **1983**, *78*, 6928−6939.

(49) Parrinello, M.; Rahman, A. Polymorphic Transitions in Single Crystals: A New Molecular Dynamics Method. *J. Appl. Phys.* **1981**, *52*, 7182−7190.

(50) Triballeau, N.; Acher, F.; Brabet, I.; Pin, J. P.; Bertrand, H. O. Virtual Screening Workflow Development Guided by the "Receiver Operating Characteristic" Curve Approach. Application to High-Throughput Docking on Metabotropic Glutamate Receptor Subtype 4. *J. Med. Chem.* **2005**, *48*, 2534−2547.

(51) Yu, A. Z.; Yu, A. B.; Dadayan, A. K.; Myasoedov, N. F. Isotopic Effects in the Electronic Spectra of Tryptophan. *Amino Acids* **2006**, *31*, 403−407.

(52) Izrailev, S.; Stepaniants, S.; Isralewitz, B.; Kosztin, D.; Lu, H.; Molnar, F.; Wriggers, W.; Schulten, K. Steered Molecular Dynamics. In *Computational Molecular Dynamics: Challenges, Methods, Ideas*, 1st ed.; Deuflhard, P., Hermans, J., Leimkuhler, B., Mark, A. E., Reich, S., Skeel, R. D., Eds.; Springer: Berlin, 1999; Vol. 4, pp 39−65.

(53) *YASARA*. http//www.yasara.org (accessed May 27, 2013).